AIAA JOURNAL
Vol. 41, No. 7, July 2003

Numerical Study of Detailed Flow Affecting a Direct Measuring Skin-Friction Gauge

Matthew MacLean* and Joseph A. Schetz†
Virginia Polytechnic Institute and State University, Blacksburg, Virginia 24061

The detailed flow characteristics of a direct measuring skin-friction gauge are examined. This type of device uses a small, movable head mounted flush to a wall, such that the head is assumed to be exposed to the same shear stress from the flow as the surrounding wall. The resulting deflection can be monitored by instruments such as strain gauges mounted on a flexure below the head. The goal of this study was to develop an understanding of the effects that the geometric design and installation parameters of the device have on the surrounding flow and the ability of the gauge to reflect the undisturbed shear stress value. Factors influencing the performance of a skin-friction gauge include the presence of the necessary gaps in the wall around the floating head, improper installation/misalignment issues with respect to the wall, and extraneous forces arising from pressure gradients. All of these effects are studied here computationally with a three-dimensional, Navier–Stokes code based on the finite element technique. It was found that smaller gap size does indeed produce the highest quality of measurement output because a larger gap results in increased exposure of the device to the external flow. Results presented here indicate that misalignment is the most significant factor that must be controlled and that it can induce an error of more than a factor of two in the measurement for the conditions studied. Finally, the configuration studied here exhibits errors of 17% or less under both strong favorable and adverse pressure gradient situations, despite the complex force fields placed on the head in these situations.

Nomenclature

A	=	area
a	=	moment arm length
b	=	normal force moment arm length
C_F	=	skin-friction coefficient
C_L	=	lip force coefficient
C_M	=	total force coefficient
C_N	=	normal force coefficient
c	=	lip size
D_{beam}	=	beam diameter
D_{head}	=	head diameter
F_X	=	tangential force
F_X^*	=	normalized tangential force
G	=	gap size
h	=	domain height
L_{beam}	=	beam length
L_{plate}	=	plate or wall length
M_Z	=	bending moment about the z axis through the center of the gauge head
M_Z^*	=	normalized bending moment about the z axis through the center of the gauge head
Re_X	=	wall station Reynolds number
u_*	=	friction velocity
x	=	coordinate in flow direction, positive in downstream direction
y	=	coordinate normal to wall surface, positive outward
y^+	=	law of the wall scale, $\rho y u_* / \mu$
Z	=	misalignment
z	=	coordinate in side direction, normal to gauge symmetry plane
Λ	=	head taper angle
μ	=	fluid viscosity
ρ	=	fluid density
τ_W	=	wall shear stress

Superscripts

$*$	=	dimensionless quantity
$+$	=	wall unit quantity

Introduction

THE direct measurement method of skin friction is one established technique for obtaining a local value of skin friction. Some of the many advantages to this method are that, in principle, it requires no advance knowledge of the general flow and that it is a conceptually simple measurement to make and postprocess.[1] Figure 1 illustrates the principle behind the direct method, showing a schematic, two-dimensional view of a typical floating (sensing) head and flexure. The action of a viscous fluid in motion over the wall applies a shear stress tangent to the wall surface. The small breaks, or gaps, in the wall region isolate a piece of the wall of known area. The flexure can be instrumented with strain gauges or displacement sensors to measure the resulting structural effects of the applied shear force. This information gives a measurement for the average shear stress over the head area.

This type of device is contrasted with the other broad class of skin-friction gauges, indirect methods. Indirect methods are various devices that operate by measuring something other than skin friction and then relating this quantity to skin friction through a known analogy or law. A few examples include: heat flux sensors with Reynolds analogy, Preston tubes, or laser/particle image velocimetry techniques. The direct method is preferred by these authors for its ability to measure skin friction directly, without any need for validating the flow analogy required by these devices. This is an important issue in complex flows such as three-dimensional flows, unsteady flows, flows over rough surfaces, etc. Brown and Joubert[1] and Winter[2] talk extensively about indirect methods, and no further discussion of these devices is presented here.

Direct measurement skin-friction gauges have been used in a wide variety of applications with apparent success. One can consult

Received 28 May 2002; revision received 23 January 2003; accepted for publication 24 January 2003.

*Graduate Research Assistant, Aerospace and Ocean Engineering Department; currently Senior Research Scientist, Calspan–University at Buffalo Research Center, 4455 Genesee Street, Buffalo, NY 14225. Member AIAA.

†Fred D. Durham Endowed Chair, Aerospace and Ocean Engineering Department. Fellow AIAA.

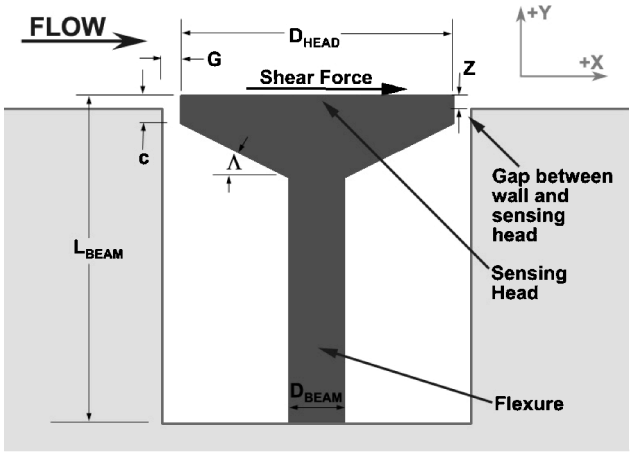

Fig. 1 Schematic of a typical, nonnulling, direct measuring skin-friction gauge showing relevant design parameters (not to scale).

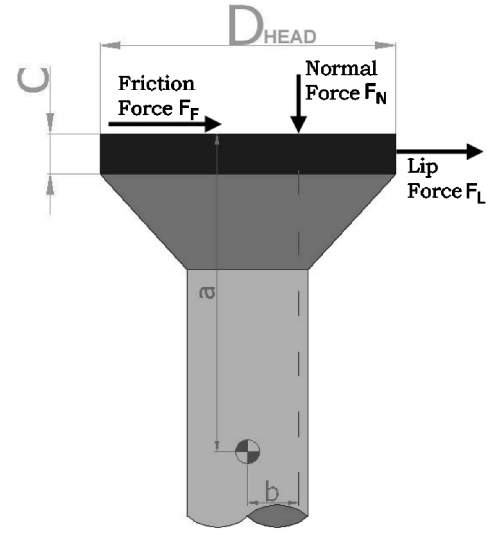

Fig. 2 Schematic of a typical, direct measuring skin-friction gauge illustrating relevant forces and moment lines of action (not to any particular scale).[7]

a number of surveys of this technique, for example, Winter,[2] Haritonidis,[3] Schetz,[4] Nitsche et al.,[5] etc., for details of some applications. There are two types of direct measuring gauges, both of which have been used in the past. Figure 1 shows a nonnulling flexure, meaning that the flexing beam bends slightly under load, as already discussed. The alternate type is a nulling gauge, in which the structural deflections are countered to maintain the nominal position of the device. Measurement in the nulling case is made by tracking the necessary reaction force to maintain position. Nulling gauges are a classical design used in instances where large deflections were required to accommodate measurement sensitivity. This led to concern about disrupting the flowfield. With modern sensors and measurement systems, the required deflections of the beam have become insignificant compared with the gap size, and no further distinction will be made here between these two types of sensors.

The direct method, in general, is appealing, but it does raise some concerns. Although it is a conceptually simple process to obtain a measurement, there is one critical assumption made. This assumption is that the shear stress present on the head surface is the only force on the structure and that it correctly represents the equivalent shear force on the solid wall section that the gauge replaces. Because the wall has gaps in it that expose the flexure to the flow, the entire skin-friction gauge is immersed in fields of pressure and shear stress. These pressure and stress fields can cause unwanted forces on the sensor and contribute to an error in the measurement. Additionally, the presence of the gaps has the potential to disrupt the flow conditions in the region around the floating head and change the local value of shear stress from the solid wall condition.

Figure 1 also shows the variable definitions used throughout this study with respect to this type of device. The focus will primarily be on the effects of the design and orientation of the floating head on the ability of the gauge to capture the desired undisturbed shear force measurement. The cantilever beam flexure shown below the head is the simplest type of flexure and was used as an example here. Although there are other arrangements that are possible, most of our results do not depend on the choice of flexure arrangement in the gauge. These variables have been deemed as the basic set that will govern the design of the majority of gauges, in principle. Different combinations of these variables will be studied parametrically here to evaluate their effects on the accuracy and performance of the device.

Winter[2] provides one of the clearest accounts of the issues and error sources associated with these devices that might change the total value of force that the gauge measures. Winter cites 10 problems for consideration; some of those problems are repeated here: 1) the effect of the necessary gaps in the wall around the floating head, 2) the effect of misalignment of the sensor (normal to the wall) such that protrusion or recession of the sensor occurs relative to the surrounding surface, 3) the extraneous forces arising from pressure gradients, and 4) the effects of leakage of flow through the sensor cavity. These four issues were selected for study here based on the justification that they seem to be some of the most fundamental or frequently occurring issues from Winter's longer list.

Because of the importance placed on making accurate measurements of skin friction, some research on error sources and magnitude has been published before. MacLean[6] provides a more extensive review of the existing literature on errors in direct skin-friction measurement, but a brief overview of some of the major conclusions is warranted here. The work of Allen[7] is well known and often referenced. He studied the effects of misalignment at supersonic speeds along a zero pressure gradient flat plate. One of his significant contributions in the study of these devices is in his modeling of the forces on the floating head of the gauge. His postulation was that the net effective force on a floating head, like that shown in Fig. 2, could comprise three terms. When the moments created by the action of these forces about the beam base or flexure pivot point are summed and the resulting equation is placed in coefficient form, Eq. (1) can be developed:

$$C_M = C_F + (b/a)C_N + (1 - c/2a)C_L \tag{1}$$

Equation (1) shows the total moment coefficient on the beam, which represents the actual output of the gauge. This output is made up of the friction force term, the normal force term, and the lip force term. The friction force term is the shear force that is the target of the measurement (in the absence of any disruptions by the gaps). This force acts in the positive x direction shown by Fig. 1. The normal force term acts in the y direction and arises from pressure variations in the flowfield that result in the pressure normal to the head surface acting axially in an eccentric manner on the flexure and contributing to bending. The lip force term also arises from a varying pressure in the flow at different points in the gap region. These devices are made such that the beam flexure is much smaller than the head. This has the effect that the cavity of the gauge is an open region, and the pressure must be approximately equal throughout the cavity region. Thus, the effects of pressure differences in the flow direction are limited mainly to acting over the lip region only, as indicated in Fig. 2 by the variable c. This term also contributes to bending on the flexure because it acts in the same direction as the friction force.

The main results of Allen's[7] tests showed that the normal and lip force terms are small at perfect alignment. For either a protruded $(+Z)$ or a recessed $(-Z)$ floating head, however, these terms become significant, and they cause a deviation between the friction force term C_F and the actual measured term C_M. In the range he studied, Allen found discrepancies in excess of a factor of 6.0 between the desired and the actual outputs. Some of his additional major conclusions were that protrusion and recession are equally

damaging to the measurement and that a larger gap size makes the gauge less sensitive to these misalignment effects.

There are other notable authors as well. Dhawan,[8] who studied the effects of the gaps in the walls, found that he could detect no discernable disruption in the boundary-layer characteristics as a result of a gaplike slot on a flat plate. Archarya et al.[9] tried to visualize the flow through the cavity and the changes as a result of the gaps around the sensing head by using smoke visualization. This experiment also produced no noticeable results, and they concluded that the effects of flow disruptions in this region must be negligible. Everett[10] studied the effects of pressure gradients (also called buoyancy effect in the context of skin friction) in a fully developed channel. O'Donnell and Westkaemper[11] also studied misalignment issues and found that even small misalignment values had a significant impact on the output of the gauge.

Note that these studies, and, indeed, all others that have been located[6] are purely experimental. Furthermore, much of this work was done using nulling-type gauges, or gauges that do not represent the general physical dimensions that are typical of current gauge designs. The present writers have not seen any other research on error sources in the direct measurement of skin friction that is computational in nature.

Problem Description

The results presented here have been obtained by the use of a computational fluid dynamics (CFD), finite element-based commercial code called FLOTRAN by Ansys, Inc. The code is a full Navier–Stokes solver in two and three dimensions with κ–ε turbulence models available. The choice of CFD over experiment has been made because it is felt that CFD offers a different point of view to contrast existing experimental results. With CFD, it is also possible to better isolate, measure, and visualize subtle flow effects that are too small for experimental devices to see, for example, flow rates through the small gaps that were not measurable experimentally.

Although the field of direct measuring gauge design is unified in the conceptual approach of finding shear stress, there is an incredible variation in size, shape, and implementation. Gauges in the past have ranged from in excess of 450 N (100 lb) (Ref. 7) to the micromachining level.[12] There have also been many variations on the cantilevered-beam theme, resulting in various support structures that are loaded in different ways. With such diversity, it is difficult to be universal in making a study of this nature. Fortunately, the nature of computational modeling inherently offers some generality. Furthermore, every effort has been made here to perform as generic an analysis as possible, to make the results that have been obtained valid for a wide range of situations.

To evaluate the performance of the generic sensor shown in Fig. 1 and to determine the amount of error it might see, some relatively simple flow conditions have been chosen in which to model typical sensor operations. These flow situations have been selected purposely for a number of reasons. First, as will be seen, the physical situations are straightforward, such that the exact solution for skin friction is either analytically predicted or at least well documented and well understood. This is important because evaluating the error in a shear stress measurement is difficult if the flow physics are so complex that the nominal value is not known. Second, everyone wants to measure skin friction in a different situation, and so some basic typical flows have been selected to try to represent, in some way, the effects seen in a large body of problems.

The first problem of interest that has been studied is that of an incompressible, laminar flow in a two-dimensional channel. Fully developed flow was generated in the long, two-dimensional channel. The working fluid was glycerin ($\mu = 1.41$ Pa · s at 298 K), and the pressure gradient studied was approximately −33,500 Pa/m in dimensional terms. The viscosity of glycerin is such that an analytical solution for shear stress of 105 Pa existed along the walls for this channel configuration. The results of this case are covered in detail by MacLean and Schetz[13] and MacLean.[6] Interested readers should see those references for results of the laminar channel cases.

The second class of problems studied represents one step up in complexity. The performance of a generic gauge mounted on a flat plate in turbulent, external flow has been considered. This problem is also incompressible, but the external flow is fully turbulent, with the center of the head of the gauge located at a Reynolds number station $Re_X = 1.7 \times 10^6$ on the flat-plate surface.

The numerical, Navier–Stokes, solution of the two-dimensional, global, flat-plate flow (with no gauge in the wall) was compared with some well-documented, experimental correlations for smooth flat plates. The agreement was found to be good over the length of the two-dimensional, global problem domain, but small biasing discrepancies in the turbulence modeling of the CFD solution and discrepancies between the various correlations preclude the use of one of these correlations for determining the target skin-friction value. Because of this, it is necessary, for consistency, to use the numerical result to obtain the predicted target value of undisturbed shear stress for error comparison with the gauge cases. This target value of C_F is 0.00307 for this case at the proper flat-plate station.

Because of the inherent complexity of turbulent flows and the need for many points very near the wall, this flow problem has been studied by the use of a combination of two- and three-dimensional methods. The global flat-plate problem without the gauge is a two-dimensional one, with the actual sensor generating only a small area where three-dimensional effects might play a role. Therefore, the information from the global two-dimensional model for the flat-plate only solution was used to generate inlet information for an embedded three-dimensional region containing the gauge. Figure 3 shows the mesh of this embedded three-dimensional region surrounding the gauge for the baseline configuration mesh. The profile information (u, v, κ, and ε) was collected from the global flat-plate solution and applied uniformly in the third plane across an inlet at a suitable distance upstream from the three-dimensional cylindrical gauge. Other usual boundary conditions apply (no slip at walls, free conditions at the top and outflow surfaces, symmetry, etc.). This embedded region concept holds for cases such as this because of the parabolic nature of the boundary layer, where knowing the solution at any station allows all downstream effects to be calculated. Thus, the solution upstream of the gauge itself is not affected by the presence or absence of the three-dimensional gauge.

The point spacing normal to the wall was kept the same between the two-dimensional global and the three-dimensional embedded region problems to avoid any interpolation near the wall where flow quantities are highly sensitive. This point spacing near the wall surface was determined from a careful, systematic study of the turbulence model wall formulation available in FLOTRAN. This code uses a two-option wall function by implementing specialized wall elements. The wall element location is determined to be within either

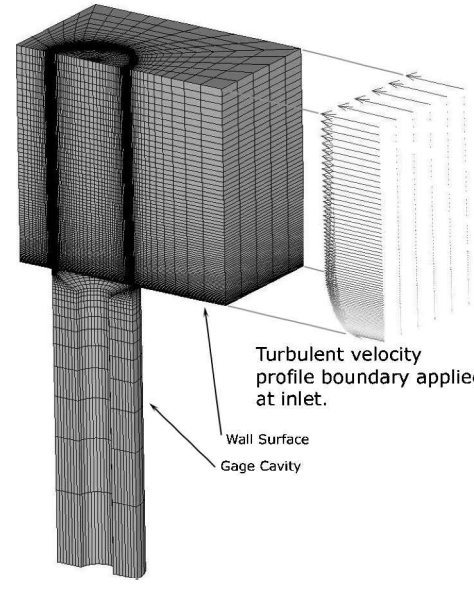

Fig. 3 Finite element mesh of embedded three-dimensional region near the gauge for baseline configuration of external flat-plate problem.

Table 1 Dimensionless value of relevant geometry and properties for baseline external flat-plate case

Parameter	Value
Re_X plate	2.0×10^6
D^+	1991.0
G^+	33.2
c^+	66.3
Z^+	0.0
Re_X gauge	1.7×10^6
D^+_{beam}	829.0
L^+_{beam}	6635.0
Λ	30 deg
C_F^{target}	0.00307

the log region or the laminar sublayer of the boundary layer, and appropriate wall conditions for the κ–ε model are generated. Analysis revealed that a y^+ spacing of the near-wall node of about 15.0 produced the best results because this spacing placed points above the near-wall node (the second and higher away from the wall) clearly into the log region ($y^+ > 30$) while maintaining maximum resolution near the wall to evaluate the effects of the small gaps. Nodes other than the near-wall node are solved for using the κ–ε equations. Therefore, they must reside well within the log region. The issue of the turbulence model selection and wall formulation details can be found in Ref. 6.

With the target skin-friction coefficient known from the flat-plate solution, the geometry of the baseline configuration of the external flat-plate problem shown by Fig. 3 is given in Table 1 in terms of wall units (+ units). This dimensionless unit form is given by Eq. (2) and defined just as the commonly used y^+ is defined:

$$()^+ \equiv ()u_*/v = [\rho()U_e/\mu]\sqrt{C_F/2} \tag{2}$$

Providing all data and generating all results in dimensionless form offers the utility of making the solutions applicable to a larger body of problem situations. The results of this baseline case illustrate typical performance of this gauge configuration and serve to provide a reference point to compare to other cases, in which the design parameters from Fig. 1 were varied. Variation cases involved making subtle changes to one or more of the design parameters to evaluate the changes from the baseline case. These design parameter changes were accounted for by varying the three-dimensional embedded meshes accordingly. The computational models of these variation cases look quite similar to the baseline case that was already shown in Fig. 3.

The results of design parameter variation from this external, turbulent flat-plate scenario were then supplemented with similar flow models possessing an adverse or favorable pressure gradient rather than the zero pressure gradient of the flat plate. The baseline configuration was studied under these two conditions by modeling high Reynolds number channels of linearly varying area. The station Reynolds number Re_X of the gauge along the channel walls was closely matched to the flat-plate case to facilitate comparison of the results. The conditions of the pressure gradient channel cases were picked such that the skin-friction levels were significantly different than the flat-plate case. The strength of the pressure gradient was determined in dimensionless terms through the use of a pressure gradient parameter, originally used in the characterization of turbulent boundary layers by Clauser[14]:

$$\beta = \frac{\delta^*}{\tau_W}\frac{\mathrm{d}P}{\mathrm{d}x} \tag{3}$$

The same embedded region technique was used in the pressure gradient cases as in the flat plate. By the use of the global solution data to get u_* and the parameters required for Eq. (3) for the gauge location, the dimensionless parameters and flow conditions for each of these two cases in wall units are given in Table 2. The reader is referred to Table 1 for comparative flat-plate data.

One final note on problem presentation concerns the form in which the major results are presented. One of the primary items of interest for these cases is the total force levels on the flexure compared to the desired shear force. The coordinate system adopted for this purpose defines the positive x direction in the flow direction, positive y normal to the head pointing out into the main flow, and z perpendicular to the flow plane. The moment center about which the flow is presented is the center of the floating element head. Equations (4) and (5) give the dimensionless forms of the global force values of interest:

Table 2 Dimensionless values of relevant geometry and flow properties for favorable and adverse pressure gradient turbulent channel cases

Parameter	Favorable pressure gradient (converging channel)	Adverse pressure gradient (diverging channel)
C_F^{target}	0.00384	0.00224
β	2.61	−0.44
Re_X gauge	1.7×10^6	1.7×10^6
Re_X plate	2.0×10^6	2.0×10^6
D^+_{head}	2226.0	1700.0
D^+_{beam}	927.0	708.0
L^+_{beam}	7421.0	5668.0
c^+	74.2	56.7
G^+	37.1	28.3
Λ	30°	30°
Z^+	0.0	0.0

$$F_X^* = F_{X,\text{total}} \Big/ \tau_W^{\text{target}} A_{\text{head}} \tag{4}$$

$$M_Z^* = M_{Z,\text{total}} \Big/ \tau_W^{\text{target}} A_{\text{head}} D_{\text{head}} \tag{5}$$

In each case, the force is divided by the target shear stress from the global two-dimensional solution times the known gauge head area. This represents the ideal, undisturbed shear force on the gauge. The z-direction moment is additionally divided by the head diameter. There is also the possibility of a force in the y direction on the beam, but this force acts axially on the beam and does not contribute to bending characteristics or to total measured output. MacLean[6] tabulates the results of this force component also for cases in which the axial force might somehow be relevant. Because both the F_X^* force and the M_Z^* moment simultaneously contribute to bending in the cantilevered pivot element shown in Fig. 1, it is also beneficial to look at the total error in output caused by a combination of these two values. This total error in strain output caused by the extraneous forces and moments is given by

$$\%\varepsilon_{\text{error}} = F_X^* - \left(D^+_{\text{head}} \Big/ L^+\right) M_Z^* - 1 \tag{6}$$

Allen[15] has shown that it is possible to mitigate the effects of the normal pressure force contributing to the z-direction moment about the head center by implementing a parallel linkage system rather than the cantilever pivot. Results of this present study have shown that the geometry inside the gauge cavity has a negligible effect on the force levels seen by the floating head. Data will be provided in later sections that divide the force and moment contributions up by their respective sources. The results might be applied to a parallel linkage system as well by simply neglecting the appropriate moment term and recomputing the total strain level via structural mechanics. For that situation, Eq. (6) will not be strictly valid. Remember that the relevant forces and moments still reside on the gauge, and the total loading on the floating head remains the same; the parallel linkage measurement system is simply not sensitive to certain features of the loading.

Turbulent Flat-Plate Boundary-Layer Results

Looking at the flowfield results from the baseline case, one sees that there is a significant flow in the gap region of the gauge, despite the small size of the gaps. Figure 4 shows the vector field in the gap regions along the gauge symmetry plane of the baseline case. Flow velocities on the order of 5% of the freestream exist within the gap regions, but much of this flow remains trapped in this gap area.

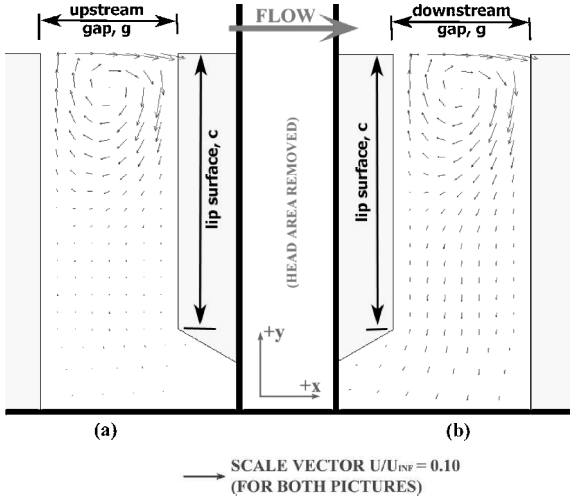

Fig. 4 Velocity vector field in the gap region along gauge symmetry plane for baseline case (boundary-layer flow left to right).

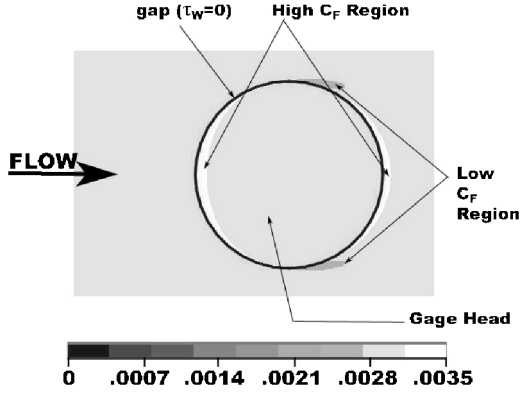

Fig. 5 Variation of wall skin-friction coefficient in gauge region for baseline case (target C_F = 0.00307).

Only a small fraction of this total flow actually moves into or out of the cavity. Interestingly, Fig. 4 shows that, in both the upstream and downstream gap area along the symmetry plane, the flow moves into the cavity (a negative y velocity component) with some small flow rate of less than 1% of the freestream velocity. A larger positive value of the y velocity component exists near the outside edges of the gauge to balance the mass flow.

This flow pattern has a direct result on the shear stress field over the wall in the floating head region. Figure 5 shows this field in coefficient form for the gauge head and the surrounding wall surface for the baseline case. As a direct result of the injection from the cavity out into the main boundary layer, the local skin-friction coefficient on the wall trailing the outer edges of the gap shows a significant decrease. This is known to be a general property of injection.[16] Fortunately, this change occurs on the surrounding wall and not on the gauge head surface itself. The gauge head shows a relatively undisturbed and constant skin-friction coefficient that is close to the target value of 0.00307. A small local increase can be seen near the leading edge, but this acts over a small percentage of the total head area and, thus, is expected to contribute only minimally to error in the friction force component defined in Eq. (1).

For this case, where the external flow conditions have a nominally zero pressure gradient, Fig. 6 shows that the pressure on and around the head surface and the lip surface of the gauge exhibit little deviance from this expectation over most of the gauge body. The pressure contours remain uniform and close to a relative pressure of zero with the exception of a small region near the leading edge of the lip surface. In this region, despite that the gauge is sheltered within the wall and the wall is under a boundary-layer flow, the leading edge of the floating head shows signs of a stagnation region, where a small amount of dynamic pressure energy is slowed to a stop against the lip surface. This dynamic pressure shows a maximum of only approximately 2% of the freestream dynamic pressure and it again acts over only a small area of the gauge body. Although this effect will be seen to contribute to the lip force term defined in Eq. (1), its influence will be shown to be manageable.

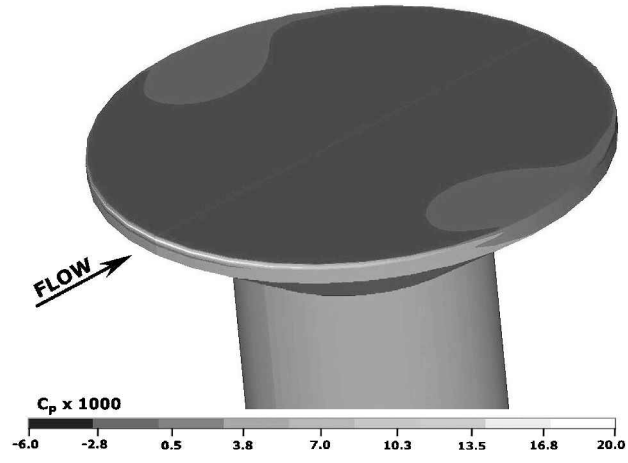

Fig. 6 Contours of pressure seen from upstream side of three-dimensional floating gauge head for baseline case.

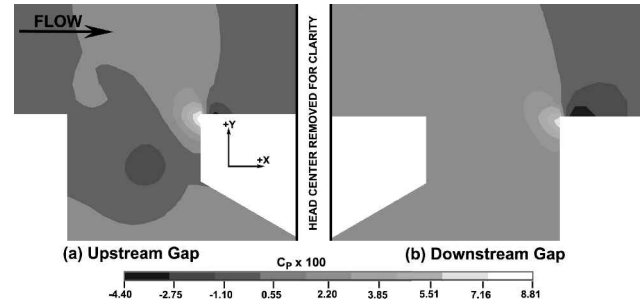

Fig. 7 Pressure contours seen along gauge symmetry plane for gap regions of maximum gap size variation case (G^+ = 132.8).

In looking at the flowfields produced by varying the gap from the baseline configuration, one does see an effect caused by an increase in gap size. The effect of the gap size was studied with cases having two and four times the baseline gap size. In these cases, the flow pattern is similar in form to the baseline case, but the magnitude of the flow is much higher. The increased flow rate in the gap region results in a higher stagnation pressure along the leading lip edge of the floating head. This effect is shown by Fig. 7, which gives pressure contours along the symmetry plane of the four times gap size case. The pressure contours over the three-dimensional surface are again similar in form to the baseline case, but the symmetry plane clearly shows the influence of the stagnation point in the upstream gap region, which is approximately four times more significant than the baseline case.

Misalignment was shown to be a primary influence on gauge accuracy by MacLean and Schetz.[13] The protrusion case of $Z^+ = +19.9$ shows the basic features that one might expect for a very short cylinder intruding out into the flow. A wake develops behind the cylinder as the flow is forced around the sides and over the top of the floating head. Figure 8 shows selected velocity vectors at a height just below the top of the surface of the cylinder to illustrate this. At this station normal to the surrounding wall, the floating head is present in the flowfield. The wake affects only the region behind the head directly, but the presence of this wake indicates that large pressure differences will be present on the head itself, and the lip force will have a dominant effect on the total output of the device. In fact, the pressure contours on the surface of the gauge head have a similar pattern to the baseline case shown by Fig. 6, but the magnitude of the stagnation region on the leading edge of the lip surface for the protrusion case is magnified by a factor exceeding 12 over the baseline case.

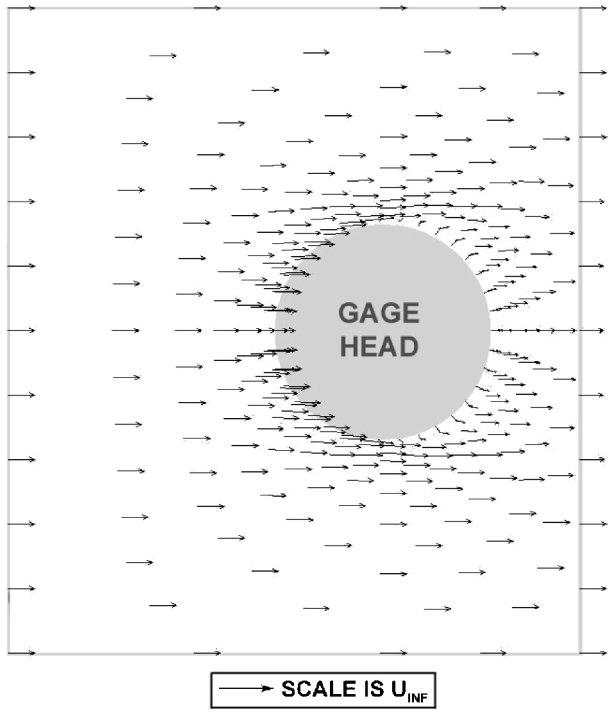

Fig. 8 Velocity vectors at a station, $y^+ \approx 13$, above the plate wall and below the gauge head for protrusion case, $Z^+ = 19.9$.

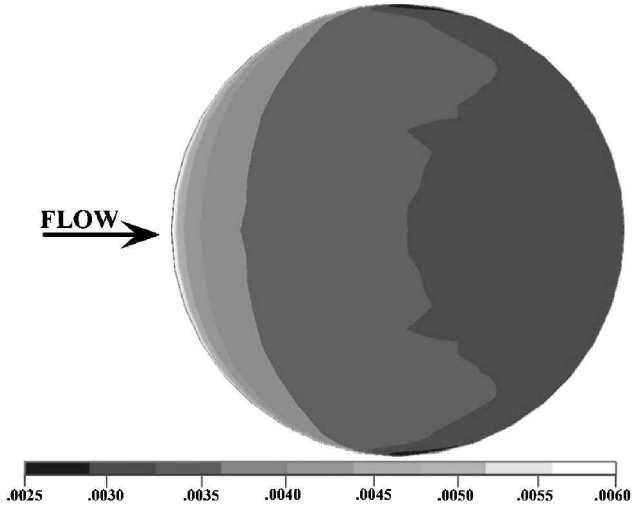

Fig. 9 Variation of skin-friction coefficient on gauge head for protrusion misalignment case, $Z^+ = 19.9$.

The effect of the presence of a wake region for the protruded misalignment cases can be important when using several gauges or sensors in the same area. The wake represents a disruption of the boundary layer in the region, which will affect the performance of any gauges (skin friction or otherwise) that are located downstream of the misaligned head. Figure 5 showed that a perfectly aligned sensing head creates almost no disruption of the boundary-layer characteristics beyond a few gap widths. This study has been concerned with the effects of misalignment on the misaligned floating head itself and, thus, made no detailed calculations of the secondary flowfield effects far downstream. However, Fig. 8 illustrates that these effects are felt over a much larger region for large misalignment levels. Any device located within a few diameters of the misaligned skin-friction gauge could be compromised. This is an aspect of skin-friction gauge implementation that deserves further consideration in future study, but the basic information seen here underscores the importance of well-aligned gauges.

Skin friction is similarly affected by the protrusion of the gauge head out into the main flow region. Figure 9 shows the skin-friction coefficient on the head surface. The surrounding wall is not shown as it was in Fig. 5 because the floating head is above the wall for this case (and not in the same plane). The skin-friction coefficient reaches values up to twice the target level near the leading edge, and the bulk of the surface shows C_F values significantly higher than the target value of 0.00307. Thus, the protruded head case will show a contribution by both shear stress and pressure in excess of the desired level to the x-direction force.

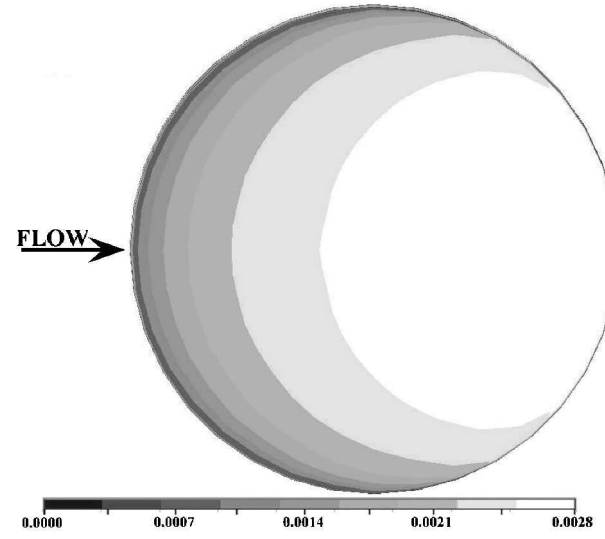

Fig. 10 Variation of skin-friction coefficient on gauge head for recession misalignment case, $Z^+ = -19.9$.

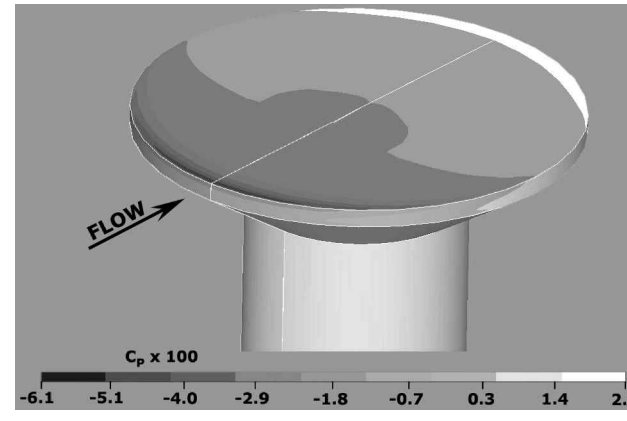

Fig. 11 Pressure contours over three-dimensional gauge surface for recession misalignment case, $Z^+ = -19.9$.

Recession misalignment also shows large discrepancies from the target value of skin-friction coefficient. In this case, as Fig. 10 shows, the levels are too low. The maximum value of C_F seen anywhere on the surface of the gauge is only 0.0028. Because of the sheltering of the head by the upstream wall, much of the head surface sees even lower values than this. In this case, shear stress is underrepresented in the x-direction force total.

The recessed head case also shows a complex pressure field operating on the gauge surface. Looking at the pressure profile over the three-dimensional surface of the $Z^+ = -19.9$ recession case shown in Fig. 11, one sees that the pressure levels are not much higher in magnitude than the levels of the baseline case. The distribution of the pressure field, however, is such that large pressure differences exist normal to the gauge surface at the extreme leading and trailing regions of the head. This effect translates to a large positive M_Z^* moment contribution for the recessed cases. This results in a negative contribution to total output via Eq. (6) for the cantilever pivot geometry.

With the flowfield results in mind, the results of the forces on the floating head can be presented and understood. Figure 12 gives

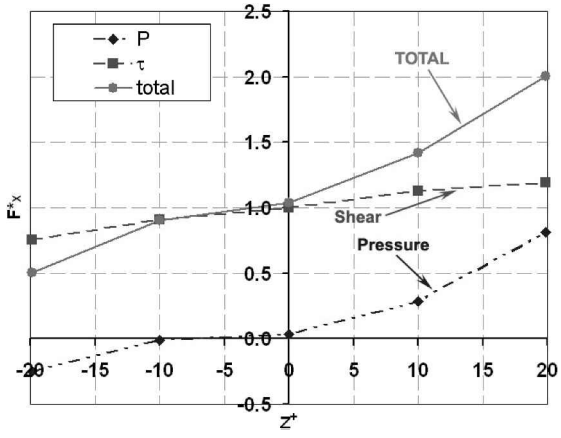

a) Force component F_x^* in x direction

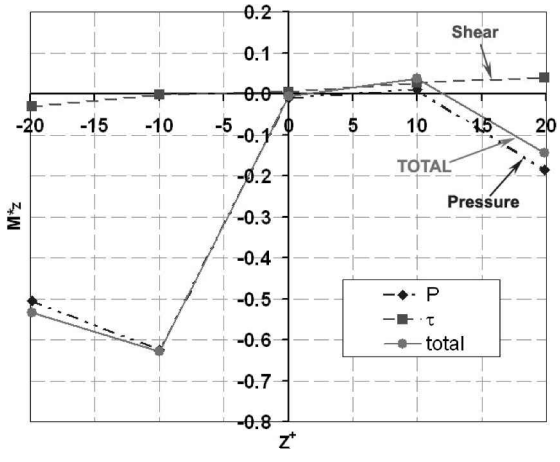

b) Moment component M_z^* for z rotation

Fig. 12 Results for variation of misalignment parameter z for external, turbulent flat-plate flow.

the results of the F_X^* force and the M_Z^* moment for the variation of the misalignment parameter Z, varied in the range from $+1$ to -1% of the head diameter. This is a Z^+ range of approximately ± 20 in wall unit terms. As the study of the flowfield indicated, the F_X^* value is close to the desired value of 1.0 for the perfectly aligned baseline case. The shear stress is undisturbed, indicating that the presence of the gap does not significantly affect the boundary layer for this baseline configuration. Also, the pressure contribution is minimal, as indicated by Fig. 6, contributing little to either F_X^* or M_Z^*. Any misalignment, however, either protrusion or recession, affects both the shear stress and the pressure field on the gauge because both the force and the moment vary considerably as a function of misalignment.

The moment graph from the pressure contribution in Fig. 12 indicates that the moment has a complex functionality with respect to misalignment. That the moment contribution from pressure first shows a small positive value and then becomes negative with increasing protrusion might at first seem counterintuitive. Although more cases are required to further refine this dependency, some credibility can be assigned to this result by comparison with available experimental data. MacLean[6] shows that transforming the numerical data from Fig. 12 to the friction force, normal force, and lip force contributions given by Eq. (1) shows good qualitative agreement with the trends found by Allen[7] in his experiments, even for this trend of moment effect from pressure. Furthermore, neglecting the pressure moment effect as one would for a parallel linkage arrangement results in a compatible result to the parallel linkage work of Allen[15] in his later experiments. Although a detailed quantitative comparison is impossible because the flow conditions and gauge geometries are very different, this result indicates that much of the physics involved in these conclusions hold for a wider range of situations.

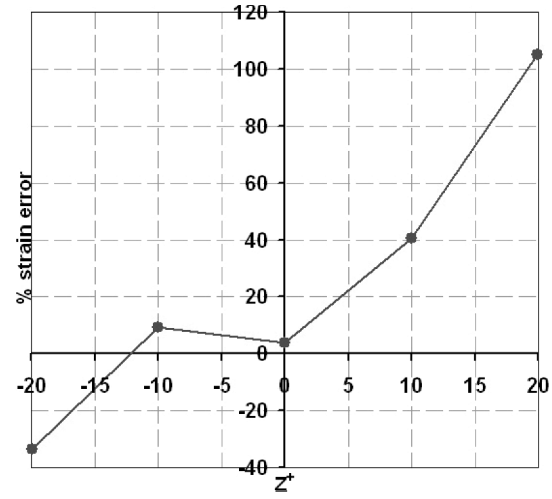

Fig. 13 Total strain output error given By Eq. (6) at flexure base for variations of misalignment parameter z for external, turbulent flat-plate conditions.

Because both F_X^* and M_Z^* contribute to total error in output for a single cantilever pivot arrangement, Fig. 13 shows the strain error output for misalignment variation caused by those two terms together. Head protrusion does indeed seem to be worse than an equal level of recession. Protrusion values Z^+, of $+20$ for this geometry and flow conditions create an error in acquired measurement in excess of a factor of two. Although the recession case shows higher magnitudes of M_Z^* values, the excess lip force caused by the pressure in the protrusion case clearly is the most damaging factor to the measurement.

Although misalignment proved to be the most significant parameter that was studied for these conditions, the size of the gap G^+, was also found to affect the measurement. Computational results from this study show that there is indeed a measurable benefit to a smaller gap size. Figure 14 gives the F_X^* force results from the gap parameter variation study. The gauge head had perfect alignment ($Z^+ = 0$) for these cases, and all other parameters except gap remained the same as the baseline case. The baseline case in this graph is compared with cases of a gauge having twice and quadruple the original gap size. The shear stress term shown in this Fig. 14 remains consistently 1.0 for all cases. This indicates that even the largest gap size does not alter the boundary layer in any significant way. This is encouraging, although the pressure term does increase with increasing gap size. This occurs because the larger gap provides less shelter for the lip surface and creates a more pronounced stagnation region on the front lip surface, as illustrated by Fig. 7. In all cases, the M_Z^* moment was close to zero and is not shown.

The strain error in output for the cantilever beam is also given in Fig. 14, which results from the change in the F_X^* pressure term given by Fig. 14. This error seems to scale linearly, and passes close to zero at a gap size of zero. A simple linear curve fit of these data provides the relation

$$\%\varepsilon_{\text{error}} = 0.182G^+ - 2.28 \tag{7}$$

This formula provides a useful estimate of the error incurred for a gauge design in the range studied, $33 < G^+ < 133$. The intercept can be neglected with little error in the estimation for moderately sized gaps. The error caused by the gap does not pass exactly through zero at a zero gap size (a solid wall with an immovable element). This conclusion indicates that very small gaps will display nonlinear error effects, and Eq. (7), therefore, should be used with caution outside the range of gap sizes indicated. This error is not as significant as the factor of two seen for misalignment, but it can still cause an error in output in excess of 20% for the range of gaps studied.

The statement made by Allen[7] that a larger gap makes the skin-friction gauge less sensitive to misalignment was also investigated for this flow condition. Figure 15 shows the resulting total strain

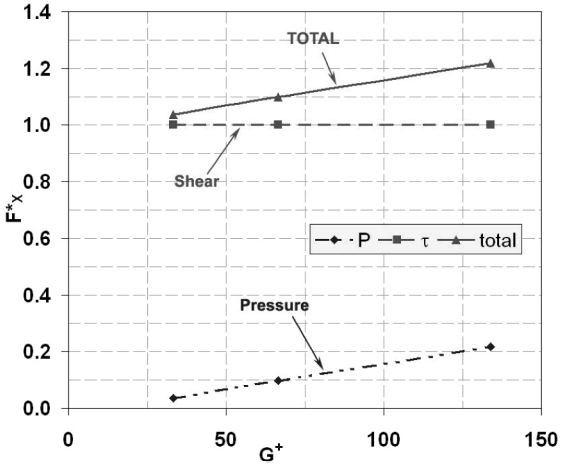

a) Force component F_x^* in x direction

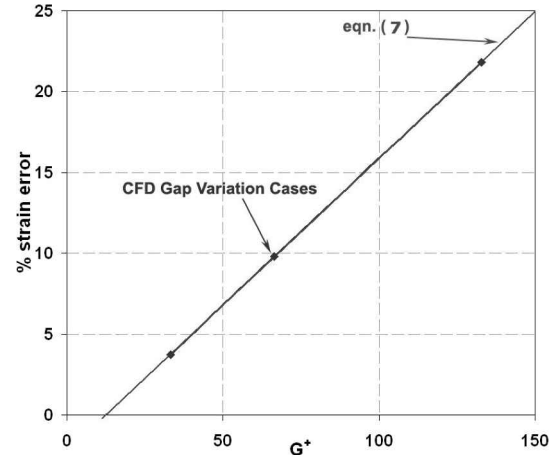

b) Output strain error and Eq. (7)

Fig. 14 Flexure base compared with approximation curve given by Eq. (7) for variation in gap parameter G for external, turbulent flat-plate flow.

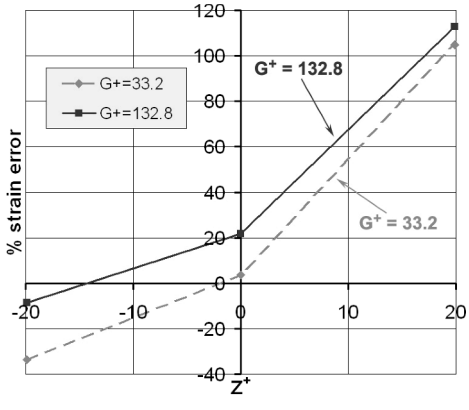

Fig. 15 Comparison of total strain output error at flexure base for small-gap and large-gap configuration as a function of misalignment parameter Z for external, turbulent flat-plate conditions.

output error for two sets of cases, the original misalignment data already presented, and a set of misalignment variations with quadruple the baseline gap size ($G^+ = 133$ or $G/D_{\text{head}} = 6.67\%$). In this case, two parameters were simultaneously varied from the baseline configuration. The result of this analysis shows that, in a strict sense, Allen's statement is indeed true. If one compares the difference in strain error between the $Z^+ = 0$ and $+20$ cases, one finds that this difference is approximately 100% for the single gap condition and 90% for the quadruple gap condition. However, the increased gap size causes the total output error to be higher than that for the baseline gap case ($G^+ = 33.2$ or $G/D_{\text{head}} = 1.67\%$). Thus, although a larger gap does seem to make the gauge less sensitive to changes caused by protrusion misalignment when compared to the perfectly aligned case, there is no benefit in doing so. In fact, the total outcome is slightly worse with the larger gap. The recession case showed about the same change from perfect alignment to $Z^+ = -20$ recession for each of the two gap configurations studied. The large $G^+ = 133$ gap condition caused a cancellation of error terms for the $Z^+ = -20$ recession case, bringing the total output closer to the target of zero strain error. However, this does not seem to be sufficient evidence to warrant making the gap larger.

On one final note, the lip thickness was also studied as a design parameter. MacLean[6] showed that this was an important parameter in the study of the laminar channel flow configuration where there is a strong imposed pressure gradient. In this case, however, where there is no pressure gradient in the flow, the lip thickness size made no difference in the simulated measurement.

Turbulent Pressure Gradient Boundary-Layer Results

The effects of imposed pressure gradients are important in the performance of a direct measuring skin-friction gauge. The flowfields in the region of the gap along the symmetry plane (upstream and downstream) are given in Fig. 16 for the converging (favorable pressure gradient) and diverging (adverse pressure gradient) channel cases. In the baseline flat-plate case, there was no globally imposed pressure gradient to drive the flow, and so much of the flow circulated within the gap region. In both of the cases with imposed pressure gradients, the flow rate through the gap is more significant, and the flow follows the direction of decreasing pressure in a much more straightforward manner. In the case of the favorable pressure gradient, the flow enters the upstream gap and exits at the downstream gap. In the case of the adverse pressure gradient, the flow pattern is

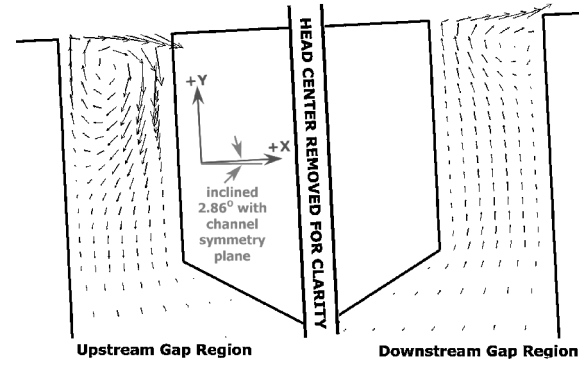

a) Favorable pressure gradient flowfield (dP/dx < 0)

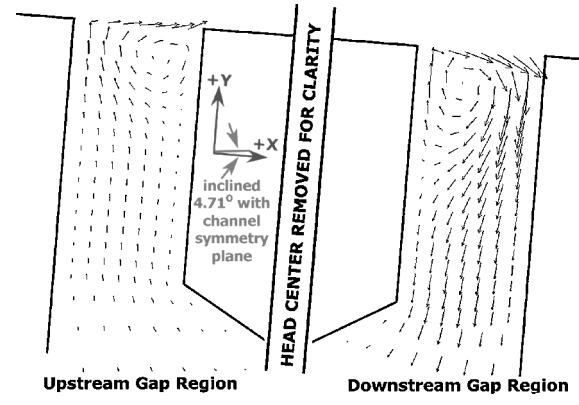

b) Adverse pressure gradient flowfield (dP/dx > 0)

SCALE V/V_{INF}=0.2 (Both Images)

Fig. 16 Arbitrarily selected velocity vectors along gauge symmetry plane for favorable and adverse pressure gradient channel cases illustrating flow profile in gap regions.

reversed, it enters the cavity at the downstream gap and exits out at the upstream gap. Although some recirculation can be seen in both cases as a result of the significant presence of convection in these two models, each case shows a definitive path and a higher flow rate through the gap than for the flat-plate baseline case.

In both of these cases featuring a perfectly aligned head and pressure gradient flow, the shear stress distribution over the exposed head surface remains unaffected. This suggests that the boundary-layer development is not disturbed by the presence of the gaps in either case, despite the changes in the boundary-layer characteristics caused by the pressure gradients in the flow.

Figure 17 shows contours of pressure coefficient over the three-dimensional head surface for the favorable pressure gradient case as seen from a generally upstream perspective. The pressure distribution over the top of the exposed head can be seen, with the pressure highest near the leading edge of the head and lowest near the trailing edge. This contributes to the normal force term from Eq. (1), which creates a positive moment in the z direction that contributes negatively to error in the total output. In addition, a similar stagnation region appears at the leading edge of the lip surface, similar to what was seen in Fig. 6 for the flat-plate case. This effect is a feature caused by the gap in the wall failing to fully shelter the floating head from the outer flow. This causes a lip force term that adds in a positive manner to the total error in gauge output.

Figure 18 shows similar three-dimensional views of the pressure variable over the head surface for the adverse pressure gradient case. In this case, the pressure increases over the length of the gauge surface, and pressure is highest at the trailing edge of the gauge. This distribution creates a negative moment in the z direction, adding to total error in gauge output. Looking at the lip surface from both upstream and downstream of the gauge, one sees that the stagnation region forms on the upstream lip surface, just as it did for the favorable pressure gradient and the flat-plate cases. Also, a wakelike region is seen on the trailing part of the lip surface. Thus, the pressure is higher on the upstream part of the lip surface despite that the pressure in the downstream part of the inviscid channel is higher. The lip surface force, which might be assumed to act in the negative x direction without detailed information, is shown to be a complex effect that is not easily intuited.

Table 3 gives the results of the integrated forces over the gauge surface for both the favorable and adverse pressure gradient cases, with the flat-plate baseline cases results given for comparison. As foretold by the stress field analyses, shear stress is well predicted in all three cases, showing a total F_X^* force close to 1.0. For the favorable pressure gradient case, the F_X^* force from pressure is 0.062, a positive contribution as predicted. In the case of the adverse pressure gradient, the lip force (F_X^* from pressure) is close to zero, 0.008, as a result of the complex effects on that surface. For the M_Z^* moment term, the favorable pressure gradient case shows a positive moment and the adverse pressure gradient case shows a similar magnitude negative moment. Both result almost entirely from pressure, as predicted by the pressure field imagery.

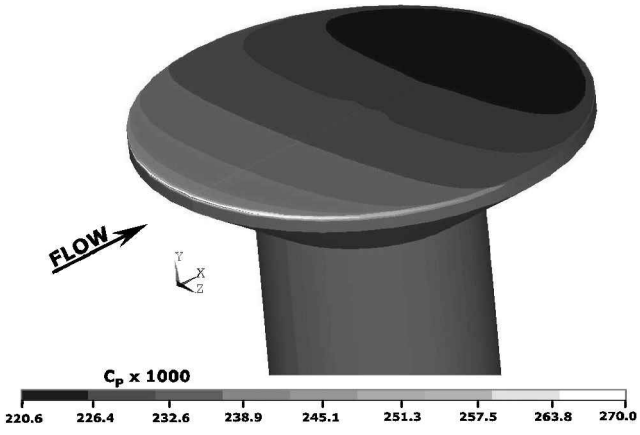

Fig. 17 Pressure contours over three-dimensional gauge surface for favorable pressure gradient (dP/dx < 0) channel case.

Table 3 Dimensionless force results for favorable and adverse pressure gradient conditions with flat-plate baseline case results for comparison

Output source	F_X^*	M_Z^*	Strain error,%
Adverse pressure gradient ($dP/dx > 0$)			
Total	1.002	−0.559	17.0
Pressure	0.008	−0.557	
Shear	0.994	−0.002	
Flat plate ($dP/dx = 0$)			
Total	1.037	0.006	4.0
Pressure	0.036	−0.010	
Shear	1.001	0.004	
Favorable pressure gradient ($dP/dx < 0$)			
Total	1.090	0.501	−6.0
Pressure	0.062	0.493	
Shear	1.028	0.008	

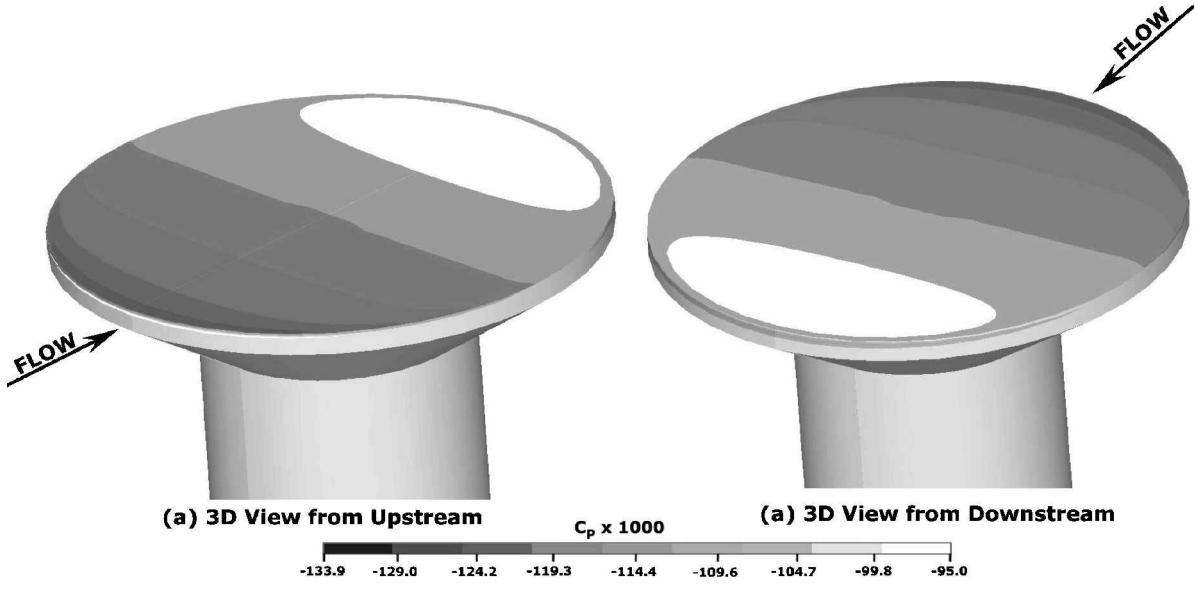

Fig. 18 Upstream and downstream views of pressure contours over three-dimensional gauge surface for adverse pressure gradient (dP/dx > 0) channel case.

The result of the force summary for the cantilever pivot in Table 3 shows that the favorable pressure gradient case predicted an output that is too low (negative) by 6.0%. The adverse pressure gradient case predicts an output that is too high by 17.0%. These data show that, counter to intuition, minimization of the lip thickness may not be beneficial for this configuration and flow condition. For the favorable pressure gradient case, making the lip thickness smaller could reduce the effect of the lip force on the total output. This means that the F_X^* contributed by pressure would decrease, which would make the output more negative and increase the total output error magnitude. For the adverse pressure gradient case, the lip force is already close to zero, and a further decrease would yield a minimal change. The conclusion based on this information is that making the lip thickness smaller would at best have no effect on the error levels and could possible be harmful. Particularly in the adverse pressure gradient case, however, the pressure profile over the lip surface is complex and difficult to predict. More study is needed on this matter to draw further conclusions.

Computational Validation and Verification

The issues of computational validation and verification were examined in detail during this work.[6] Validation, or "solving the right equations,"[17] is the issue of modeling errors in computational analysis. This describes how well the mathematical model captures the actual physical flow problem of interest. Turbulence modeling is a common modeling error, and the standard κ–ε model was used here. This choice was verified by comparing the results obtained for the baseline turbulent flat-plate case and the protrusion misalignment case with results from three alternate turbulence models, suggested by Girimaji,[18] Yakhot et al.,[19] and Shih et al.[20] Results showed good correlation within about 2.5% of the default standard κ–ε model.

The second part of computational uncertainty is verification, or "solving the equations right."[17] Convergence is discussed first. One measure of convergence is to look at the iteration history of the relevant parameters in question. Over the final 1000 iterations, it was found that the F_X^* parameter changed by only 0.00004% for the baseline external flat-plate flow case. For the favorable pressure gradient case, F_X^* showed a 0.012% difference and M_Z^* a 0.130% difference for the final 125 iterations. For the adverse pressure gradient case, F_X^* showed a 0.040% difference and M_Z^* a 0.260% difference for the final 125 iterations. Another standard measure of convergence is the value of the equation set at the approximate solution, which is referred to as a residual. Note that the residual values were found to be low enough for all cases studied here that convergence error can be neglected when compared to the ordered discretization error.[6]

Ordered discretization error, or grid convergence error, was the major contributor to computational error for all cases studied here. This is typical of most CFD applications. Richardson extrapolation was implemented as a tool to assess grid dependency, coupled with the grid convergence index (GCI).[21] The GCI is derived from the use of Richardson extrapolation over successively refined grids. The Richardson extrapolation error estimator (see Ref. 21) A_1 can be derived over two successive grids. It is then possible to calculate GCI, given as

$$\mathrm{GCI}^{\mathrm{fine}} = 3|A_1| = 3\left|\frac{(f_2 - f_1)/f_1}{\left(r_{12}^p - 1\right)}\right| \tag{8}$$

Here, f is any given degree of freedom, grid 1 is the finer grid, grid 2 is the coarser grid, r_{12} is the ratio of grid 2 element size to grid 1 element size ($r_{12} > 1$), and p is the order of convergence. It is possible to use this technique on any derived global quantity like lift coefficient or drag coefficient,[21] and it is used here for F_X^* and M_Z^*. The GCI is a very conservative estimate. Roache[22] emphasizes "that the GCIs are not error estimators but are [three] times the error estimators, representing error bands in a loose statistical sense."

Because three-dimensional turbulent boundary-layer models are computationally intensive, the grid dependency issue was studied for all of these cases based on identical two-dimensional representations of the case. It is presumed that the two-dimensional representation will be a worst case scenario. In two dimensions, the floating head is an infinite obstacle, and flow can pass only over or under (through the cavity of) this obstacle. In three dimensions, flow can move around the sides of the head in a less disruptive manner.

Table 4 Richardson extrapolation error estimators and GCI values for two-dimensional representative simulations of three-dimensional embedded region cases, F_X^*

	$\%A_1$			
Case	Shear	Pressure	Total	$\%\mathrm{GCI}_{\mathrm{total}}$
Baseline flat plate	−1.7	−61.8	−3.7	11.1
Flat plate $Z^+ = +20$	4.0	−54.4	−20.8	62.4
Flat plate $Z^+ = +10$	3.7	−55.8	−8.5	25.5
Flat plate $Z^+ = -10$	−8.7	30.3	−18.0	54.0
Flat plate $Z^+ = -20$	−2.2	−35.9	30.3	90.9
Flat plate $G^+ = +66$	4.7	−80.5	−0.3	0.9
Flat plate $G^+ = +133$	3.9	−15.3	0.1	0.3
Pressure gradient $\beta = -0.5$	−0.8	−30.5	−2.7	8.2
Pressure gradient $\beta = +3$	−2.9	198.9	−5.3	16.0

Table 5 Richardson extrapolation error estimators and GCI values for two-dimensional representative simulations of three-dimensional embedded region cases, M_Z^*

	$\%A_1$			
Case	Shear	Pressure	Total	$\%\mathrm{GCI}_{\mathrm{total}}$
Baseline flat plate	−85.2	−101.1	−102.0	306
Flat plate $Z^+ = +20$	−179.6	−40.9	−37.5	112
Flat plate $Z^+ = +10$	−147.6	−119.8	−117.6	352
Flat plate $Z^+ = -10$	32.8	44.0	43.8	131
Flat plate $Z^+ = -20$	−52.4	−5.7	−6.4	19.2
Flat plate $G^+ = +66$	−175.6	−101.5	−98.6	295
Flat plate $G^+ = +133$	−84.6	−19.3	−16.8	50.4
Pressure gradient $\beta = -0.5$	−61.6	8.2	7.5	22.4
Pressure gradient $\beta = +3$	98.9	−9.7	−5.3	28.1

Tables 4 and 5 give the grid convergence information for all cases studied here. At first glance, there is a wide range of error estimation results for the different categories. In most cases, the highest values predicted for A_1 and GCI correspond to values where that particular contribution is close to zero or of inconsequential influence on the total. For example, the shear stress in every case contributes almost nothing to the M_Z^* moment. Although the A_1 estimators for this term are all high, the total outcome is not strongly affected. The same is true with the pressure contribution to M_Z^* for the cases where the gap was varied with perfect alignment under the turbulent, flat-plate conditions. The total M_Z^* is small and does not affect the total output error significantly, despite the A_1 and GCI values.

Only in the misalignment cases does the A_1 estimator seem to be both large and important. Fortunately, these cases, where the grid dependency error is highest, are also the cases where the solution parameters show the most difference between the cases. For example, the grid dependency estimation error is predicted to be much higher for the Z^+ protrusion case of 19.9 than in the baseline flat-plate case. The total output strain error of 105% for this case, however, is large enough that the result is still significant despite the increased grid sensitivity for this case.

Finally, the boundary dependence was studied for the baseline case. Roache[22] showed that the boundary placement for some classes of problems can be shown to be first order with the distance to the boundary from the region of interest. This result is assumed to hold here as a first-order boundary dependence error means by which doubling the distance to the boundary makes the percent difference between the two solutions equal to the A_1 estimator. Doubling the downstream boundary distance produced no change in the solution parameters of interest. This is consistent with the physical parabolic nature of the boundary layer. Doubling the distance to the upstream boundary produced percent differences or A_1 estimators of 0.012% for F_X^* and 1.75% for M_Z^* for the baseline case. Although these values are measurable, they are more than one order of magnitude less significant than the errors found for the grid dependency error.

As with the convergence error, the conclusion is that this source of error can be neglected when compared to the total error. The conclusion from the extensive computational error study, given fully by MacLean,[6] is that the grid dependency (ordered discretization) error is dominant over all other sources combined by one order of magnitude or more.

Conclusions

Results of skin-friction gauge performance have been presented here for some simple, representative flow conditions. The performance has been assessed for some generic gauge parameters picked to be typical of current trends in direct skin-friction measurement design. By the use of a Navier–Stokes CFD code, this geometry was input in dimensionless form, and a corresponding dimensionless output was obtained. Although the studies presented here have been for one particular design type, all results have been given in dimensionless form here and all geometric variables given in wall coordinate units to improve the applicability to a wider range of flow conditions and gauge designs. Flow conditions that deviate significantly from these dimensionless conditions can use this study as a template for a study specifically tuned to the conditions in question.

With this approach, parameters were varied one or two at a time, and these effects were assessed. For an incompressible, turbulent boundary-layer flow over a flat plate at a Reynolds number based on plate length of 1.7×10^6, misalignment proved to be the most significant factor in performance. Results of this typical skin-friction gauge in its baseline configuration showed that the actual output from the device was within a few percent of the target (desired) output. With a misaligned gauge head, however, the actual output varied by more than a factor of 2.0 from the target output. For these conditions, protrusion exhibited generally higher output error than recession, although both conditions were shown to be damaging to the performance of the gauge.

The gap size also had an influence on the device, with a larger gap clearly creating a larger error in output. This resulted from the increasing exposure of the gauge lip surface to the outer flow, creating a stagnation region on the front of the lip that grew in magnitude with gap size. The size of the lip surface itself proved to be unimportant in this case with a flat-plate that imposes no global pressure gradient in the gauge region.

When the combined effects of gap variation and misalignment were examined, it was shown that gap size does indeed influence the gauge's response to misalignment. Although this conclusion is strictly consistent with earlier experimentation of skin-friction gauges, the results given here show that minimizing the gap size is still generally the most optimum configuration. The change in misalignment performance with a larger gap is not of sufficient benefit to warrant increasing the gap size intentionally.

Finally, the influence of favorable and adverse pressure gradients were investigated, illustrating that the dimensionless configuration studied showed acceptable performance in the presence of both pressure gradient conditions. The adverse pressure gradient case showed the largest error levels at 17%. The analysis also indicated that minimizing the lip thickness of the gauge head is not necessarily the optimum condition for all pressure gradient flows, as might be the intuitive conclusion. More study of this lip effect is needed to address this question fully.

As a general capability, CFD is a useful design and performance tool for skin-friction gauges. The use of CFD has enhanced the understanding of the physics involved in the intricate flows that interact with these devices, allowing for better design decisions and better experimental uncertainty analysis for these types of devices. This understanding ultimately leads to a better quality of experimental skin-friction measurement.

Acknowledgment

This work was supported by a grant from Luna Innovations, Inc., Blacksburg, Virginia.

References

[1]Brown, K. C., and Joubert, P. N., "The Measurement of Skin Friction in Turbulent Boundary Layers with Adverse Pressure Gradients," *Journal of Fluid Mechanics*, Vol. 35, No. 4, 1969, pp. 737–757.

[2]Winter, K. G., "An Outline of the Techniques Available for the Measurement of Skin Friction in Turbulent Boundary Layers," *Progress in Aerospace Sciences*, Vol. 18, 1977, pp. 1–57.

[3]Haritonidis, J., "The Measurement of Wall Shear Stress," *Advances in Fluid Mechanics Measurements*, Springer-Verlag, Berlin, 1989, pp. 229–261.

[4]Schetz, J., "Direct Measurement of Skin Friction in Complex Fluid Flows," *Applied Mechanical Reviews*, Vol. 50, Pt. 2, Nov. 1997, pp. S198–S203.

[5]Nitsche, W., Haberland, C., and Thunker, R., "Comparative Investigations of the Friction Drag Measuring Techniques in Experimental Aerodynamics," International Council of the Aeronautical Sciences, 14th ICAS Congress, ICAS-84-2.4.1, 1984.

[6]MacLean, M., "A Numerical Study of Internal Flow Effects on Skin Friction Gages," Ph.D. Dissertation, Aerospace and Ocean Engineering Dept., Virginia Polytechnic Inst. and State Univ., Blacksburg, VA, April 2002.

[7]Allen, J. M., "Systematic Study of Error Sources in Supersonic Skin-Friction Balance Measurements," NASA TN-8291, Oct. 1976.

[8]Dhawan, S., "Direct Measurements of Skin Friction," NACA Rept. 1121, 1952.

[9]Acharya, M., Bornstein, J., Escudier, M. P., and Vokurka, V., "Development of a Floating Element for the Measurement of Surface Shear Stress," *AIAA Journal*, Vol. 23, No. 3, 1984, pp. 410–415.

[10]Everett, H. U., Jr., "Calibration of Skin Friction Balance Discs for Pressure Gradient," M.S. Thesis, Aeronautical Engineering, Univ. of Texas, Austin, TX, Aug. 1958.

[11]O'Donnell, F. B., and Westkaemper, J. C., "Measurements of Errors Caused by Misalignment of Floating-Element Skin-Friction Balances," *AIAA Journal*, Vol. 3, No. 1, 1965, pp. 163–165.

[12]Schmidt, M. A., Howe, R. T., Senturia, S. D., and Haritonidis, J. H., "Design and Calibration of a Microfaricated Floating-Element Shear-Stress Sensor," *IEEE Transactions on Electron Devices*, Vol. 35, No. 6, 1988, pp. 750–757.

[13]MacLean, M., and Schetz, J. A., "Study of Internal Flow Effects on Direct Measurement Skin Friction Gages," AIAA Paper 2002-0531, Jan. 2002.

[14]Clauser, F. H., "Turbulent Boundary Layers in Adverse Pressure Gradients," *Journal of Aerospace Sciences*, Vol. 21, 1954, pp. 91–108.

[15]Allen, J. M., "Improved Sensing Element for Skin-Friction Balance Measurements," *AIAA Journal*, Vol. 18, No. 11, 1980, pp. 1342–1345.

[16]Schetz, J., *Boundary Layer Analysis*, Prentice–Hall, Englewood Cliffs, NJ, 1993, Chap. 7.

[17]Blottner, F. G., "Accurate Navier–Stokes Results for the Hypersonic Flow over a Spherical Nosetip," *Journal of Spacecraft and Rockets*, Vol. 27, No. 2, 1990, pp. 113–122.

[18]Girimaji, S. S., "Fully Explicit and Self-Consistent Algebraic Reynolds Stress Model," ICASE, TR 95-82, 1995.

[19]Yakhot, V., Orszag, S. A., Thangam, S., Gatski, T. B., and Speziale, C. G., "Development of Turbulence Models for Shear Flows by a Double Expansion Technique," *Physics of Fluids A*, Vol. 7, No. 7, 1992, pp. 1510–1520.

[20]Shih, T., Liou, W., Shabbir, A., Yang, Z., and Zhu, J., "A New κ–ε Eddy Viscosity Model for High Reynolds Number Turbulent Flows," *Computers and Fluids Journal*, Vol. 24, No. 3, 1995, pp. 227–238.

[21]Roache, P. J., *Verification and Validation in Computational Science and Engineering*, Hermosa, Albuquerque, NM, 1998.

[22]Roache, P. J., "Quantification of Uncertainty in Computational Fluid Dynamics," *Annual Review of Fluid Mechanics*, Vol. 29, 1997, pp. 123–160.

J. P. Gore
Associate Editor